HIGHLY RESOLVED LARGE EDDY SIMULATIONS OF A LAMINAR-TURBULENT TRANSITIONAL AIR-HELIUM BUOYANT JET IN A TWO VENTED ENCLOSURE: VALIDATION AGAINST PARTICLE IMAGE VELOCIMETRY EXPERIMENTS

E. Saikali[1,2,3], G. Bernard-Michel[1], A. Sergent[2,4], C. Tenaud[2] and R. Salem[1]

[1] *DEN/DANS/DM2S/STMF/LIEFT,*
Bât. 460, CEA Saclay,
91191 Gif-Sur-Yvette cedex, France,
e-mails : elie.saikali@cea.fr
gilles.bernard-michel@cea.fr
[2] *LIMSI, CNRS, Université Paris-Saclay,*
Bât. 508, F-91405 Orsay, France
e-mails : elie.saikali@limsi.fr
anne.sergent@limsi.fr
christian.tenaud@limsi.fr
[3] *IFD, ED391 SMAER, UPMC Paris 06,*
Sorbonne Universités, F-75006, Paris, France
[4] *UFR 919 Ingénierie, UPMC Paris 06,*
Sorbonne Universités, F-75005, Paris, France

ABSTRACT

The article deals with LES simulations of an air-helium buoyant jet in a two vented enclosure and their validation against particle image velocimetry experiments. The main objective is to test the ability of LES models to simulate such scenarios. These types of scenarios are of first interest considering safety studies for new hydrogen systems. Three main challenges are identified. The two first are the ability of the LES model to account for a rapid laminar-to-turbulence transition, mainly due to the buoyancy accelerations, and the Rayleigh-Taylor instabilities that can develop due to sharp density gradients. The third one is the outlet boundary conditions to be imposed on the vent surfaces. The influence of the classical pressure boundary condition is studied by comparing the simulations results when an exterior region is added in the simulations. The comparisons against particle image velocimetry experiments show that the use of an exterior domain gives more accurate results than the classical pressure boundary condition. This result and the description of the phenomena involved are the main outlets of the article.

NOMENCLATURE

LES	Large eddy simulations		SGS	Sub-grid scale	
DNS	Direct numerical simulations		PIV	Particle image velocimetry	
rms	Root mean square		ACF	Auto correlation function	
am	Subscript denoting ambient		in	Subscript denoting injection	
$\bar{}$	Space filter symbol		$\tilde{}$	Favre averaging symbol	
$< \cdot >_t$	Time averaging operator		D/Dt	Total derivative operator	
Ri	Richardson number	[-]	Re	Reynolds number	[-]
C_s	Smagorinsky coefficient	[-]	Sc	Schmidt number	[-]
Ma	Mach number	[-]	$\mathcal{O}$	Cartesian system's origin	[-]
Y_1	Helium mass fraction	[-]	X_1	Helium volume fraction	[-]
t	Time	[s]	δt	Time step	[s]
λ_f	Taylor micro-scale	[s]	$\mathbf{x}$	Space vector	[m]
δ	Mesh step size	[m]	Δ	Filter width	[m]
η	Kolmogorov length scale	[m]	W	Horizontal width of cavity	[m]
L	Span-wise length of cavity	[m]	H	Height of cavity	[m]
d	Diameter of pipe	[m]	h	Height of pipe	[m]
p	Thermodynamic pressure	[Pa]	P	Hydrodynamic pressure	[Pa]
τ	Viscous stress tensor	[Pa]	f	Frequency	[Hz]
$\mathcal{M}_{He}$	Helium mass in the cavity	[Kg]	T	Temperature	[K]
$\mathbf{u}$	Mixture mass velocity vector	[m.s^{-1}]	g	Gravity vector	[m.s^{-2}]
D	Mixture diffusion coefficient	[m^2.s^{-1}]	E_k	Kinetic energy	[m^2.s^{-2}]
ϵ	Total dissipation rate	[m^2.s^{-3}]	Q	Volumetric flow-rate	[m^3.s^{-1}]
ρ	Density	[Kg.m^{-3}]	q	Mass flow-rate	[Kg.s^{-1}]
M	Molar mass	[Kg.mol^{-1}]	μ	Dynamic viscosity	[Kg.m^{-1}.s^{-1}]
R	Specific gas constant	[J.K^{-1}.mol^{-1}]			

I. INTRODUCTION

Systems using hydrogen as an energy carrier are considered one of the important engineering applications that will extensively appear in our every day life over various range of scales; cars fuel cell, power generation stations ... From an environmental point of view, these systems prevent CO2 emission and thus are more efficient to use. However, such a new generation requires a careful sensitive study before coming into a widespread use [1].

The main issue is with the hydrogen gas which is initially stored inside bottles and then distributed through pipes to feed the system and to produce energy. A typical accidental situation is when hydrogen escapes inside the environment, such as a fuel cell or a garage, and rises in a form of a plume-jet which entrains air and potentially forms a dangerous-flammable mixture with hazardous consequences, due to the concentration accumulation. This issue is well presented by Cariteau et

al. in [2].

The flow regime inside the environment can be predicted and characterized by estimating the dimensionless Richardson number (Ri), which compares the buoyant-to-inertial strengths at the leakage position [3]. When $Ri \gg 1$, a pure plume regime is predicted and the flow can become turbulent after the gravitational accelerations. However, when $Ri \ll 1$, a pure jet regime is predicted to occur where turbulence originates from the inertial accelerations. The present paper aims at simulating a particular case for a Ri slightly less than unity. In this case, we predict the development of a buoyant jet where a transition from an inertial-driven jet into a buoyancy-driven plume occurs in a short distance above the leakage position [4].

From a physical point of view, the problem is considered as an intrusion of a light fluid into a heavier one, which is well known as buoyant convection from isolated sources according to the classification of Baines and Turner in [5]. As a consequence of the continuous intrusion and under specific conditions, density stratification can build-up inside the medium. Qualifying the levels of stratification is important for safety studies and is encountered in many technical and engineering applications; both in a free or a bounded media. Such applications can be seen in the study of fuel leakage in containments, jets entering mixing chambers, smokestack discharge, study of severe accident scenarios, fire modeling and ventilation [6, 7].

In the present work, the medium is assumed to be a two vented parallelepiped enclosure. We present large eddy simulations (LES) of the complete three dimensional (3D) cartesian geometry without a priori made of any axi-symmetrical assumptions. The small unresolved scales of motion are modelled by the classical Smagorinsky sub-grid scale (SGS) model with a logarithmic law near the solid boundaries. We have carried out this study after looking at different methodologies discussed in the literature. LES has shown to be a widely used tool for simulating complex turbulent flows [8]. A particle image velocimetry (PIV) experiment has been carried out at CEA Saclay in parallel with the numerical simulations. We use the experimental data to validate the obtained LES results. Taking into account the significance of the density ratio and following a security assessment, the experimental study was carried out on helium rather than hydrogen.

Buoyant jets in two vented cavities are extremely interesting and challenging configurations for several reasons. On the one hand, a rapid laminar-to-turbulence transition occurs within a few distance above the intrusion position, mainly due to the buoyancy accelerations. In addition, because of the sharp density gradients located mainly at the jet boundaries, Rayleigh-Taylor instabilities can develop and generate high fluctuations inside the medium [9]. On the other hand, there is no clear idea on the correct outlet boundary conditions that can be directly imposed on the vent surfaces and thus representing the true flow. This issue remains an open problem of research especially that a vent can have an opposite flow orientation at the same time.

The presented key-points are challenging for computational fluid dynamics (CFD) codes and justify the interest of the present study. To the authors knowledge, no similar work is reported in the literature. The aim of the paper is twofold. Firstly, to highlight on the influence of using classical pressure boundary conditions by taking into account an exterior region in the computational domain, moving the outlet boundaries away from the vents. Secondly, to understand the mixing-dispersion of the flow and to analyze the average behavior of the helium stratification inside the cavity.

A brief outline of the paper follows. The model and the numerical methods are discussed in section

two. Section three is devoted to the numerical results. Conclusions and future perspectives are drawn finally in section four.

II. MODEL AND NUMERICAL METHODS

A. Physical and numerical configurations

To study the behavior of an air-helium buoyant jet inside a two vented enclosure, an experimental study has been carried out at CEA Saclay. Pure helium is injected through a cylindrical pipe with a constant volumetric flow-rate $Q = 5$ Nl/min $\approx 9.096 \times 10^{-5} \mathrm{m}^3.\mathrm{s}^{-1}$ into a two vented parallelepiped enclosure filled initially with air at rest. Otherwise stated, the helium fluid is referred to by an $_{in}$ subscript (meaning "injected"), while the subscript $_{am}$ is used to denote the ambient air. The injection pipe is of diameter $d = 10^{-2}$ m and long enough to ensure a well developed Poiseuille velocity profile. The dimensions of the cavity are $W \times L \times H = 4.9{\times}5{\times}14.9 \times 10^{-6}$ m^3. The two vents are considered to be identical with a surface area $5{\times}2.9{\times}10^{-4}$ m^2 and both located on the right vertical wall. Plexi-glass of thickness 5×10^{-3} m is used for the solid wall boundaries. A schematic representation of the experimental set-up is shown in figure 1.

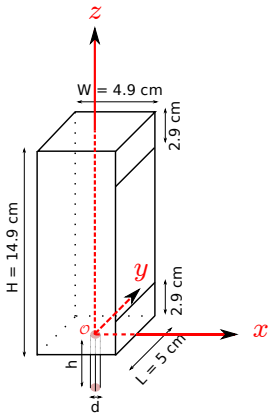

FIG. 1: Experimental set-up

Fluid	Density	Dynamic viscosity	Molar mass
	[kg.m^{-3}]	[$\times 10^{-5}$ kg.m^{-1}.s^{-1}]	[$\times 10^{-2}$kg.mol^{-1}]
Injected	$\rho_{in} = 0.16148$	$\mu_{in} = 1.918$	$M_{in} = 0.4003$
Ambient	$\rho_{am} = 1.16864$	$\mu_{am} = 1.792$	$M_{am} = 2.897$

TABLE I: Physical properties of the working fluids

We emphasize that the presented geometry has been proposed to ensure that the interesting physical phenomena of the flow are captured. In particular, the height H of the cavity was selected so as to obtain a transitional flow regime from laminar to turbulent, which is predicted to occur at $H/d \gg 5$ [3]. In addition, the length L and the width W are chosen to take into account the jet spreading angle, estimated near 11-12°, so that we avoid direct interactions between the jet and the lateral walls of the cavity [10].

The temperature T and the thermodynamic pressure p are assumed to be constant and not varying during the experiment; $T = 25°$ C and $p = 10^5$ Pa ≈ 0.98 atm. Thus, the physical properties of the working fluids can be read from table I.

Characteristics of the desired flow are given in terms of the dimensionless injection Richarsdson

and Reynolds numbers at the injection

$$\mathrm{Ri}_{in} = \frac{g(\rho_{am} - \rho_{in})\ d}{\rho_{in} u_{in}^2} \approx 0.14 \quad \text{and} \quad \mathrm{Re}_{in} = \frac{\rho_{in} u_{in}\ d}{\mu_{in}} \approx 180,$$

where u_{in} is the maximum velocity in $\mathrm{m.s}^{-1}$.

In the numerical study, the dimensions of the cavity and the two vents, in addition to the pipe's diameter d are kept the same. However, the height of the pipe h is limited to 3×10^{-2} m. We impose a Poiseuille velocity profile at the entrance (bottom) of the pipe to make sure that the velocity distribution along the pipe matches the fully developed steady state solution in the real experiment. We have verified by numerical simulations with different $h \geq 3 \times 10^{-2}$ m that no impact on the solution was recorded inside the cavity whatever the height h is.

B. Governing equations

The flow is governed by the conservation of mass, momentum and scalar species equations. The equation of state for binary gas mixture is used to determine the mixture density from the two species mass fractions [11, 12]. We emphasize that under the justified isothermal and isobar assumptions, the problem passes without the necessity of solving the energy conservation equation. Considering a Mach number $\mathrm{Ma} = 7 \times 10^{-3} < 0.1$ and a significant density ratio $\rho_{am}/\rho_{in} \approx 7.24$, the low Mach number (LMN) approximation is valid [13]. Following an asymptotic analysis, the total pressure splits into a sum of a thermodynamic pressure $p(t)$ which is uniform in space and a space-time dependent hydrodynamic pressure $P(\mathbf{x}, t)$, where $\mathbf{x}$ denotes the space coordinate vector [14].

Applying spatial filtering (denoted by $\bar{}$) and using density weighted Favre-averaged quantities (denoted by $\tilde{}$) with $\tilde{\varphi} = \overline{\rho\varphi}/\overline{\rho}$ for any considered quantity φ, the system of LES governing equations reads [9]

$$\frac{\partial \overline{\rho}\tilde{Y}_1}{\partial t} + \frac{\partial}{\partial x_i}(\overline{\rho}\tilde{u}_i\tilde{Y}_1) = \frac{\partial \overline{\xi}_i}{\partial x_i} + \frac{\partial \overline{\xi}_i^{\mathrm{SGS}}}{\partial x_i}, \tag{1}$$

$$\overline{\rho} = \frac{p\overline{M}}{RT}, \tag{2}$$

$$\frac{\partial \overline{\rho}\tilde{u}_j}{\partial t} + \frac{\partial}{\partial x_i}(\overline{\rho}\tilde{u}_j\tilde{u}_i) = -\frac{\partial \overline{P}}{\partial x_j} + \frac{\partial \overline{\tau}_{ij}}{\partial x_i} + \frac{\partial \overline{\tau}_{ij}^{\mathrm{SGS}}}{\partial x_i} + \overline{\rho} g_j, \tag{3}$$

$$\frac{\partial \overline{\rho}}{\partial t} + \frac{\partial}{\partial x_i}(\overline{\rho}\tilde{u}_i) = 0, \tag{4}$$

where $\overline{\rho}$ is the filtered mixture density, $\tilde{Y}_1$ and $\tilde{Y}_2$ are respectively the helium and air mass fractions and satisfying $\tilde{Y}_1 + \tilde{Y}_2 = 1$, $\tilde{u}_i$ is the mass average component of the velocity vector $\tilde{\mathbf{u}} = (\tilde{u}_1, \tilde{u}_2, \tilde{u}_3)$, $\overline{\xi}_i = \overline{\rho}\ D\frac{\partial \tilde{Y}_1}{\partial x_i}$ is the molecular diffusion term modeled by Fick's law with a mixture diffusion coefficient $D = 6.91 \times 10^{-5}\ \mathrm{m}^2.\mathrm{s}^{-1}$, $\overline{M} = (\sum_{i=1}^{2} \frac{\tilde{Y}_i}{M_i})^{-1}$ is the mixing molar mass where $M_1 = M_{in}$ and $M_2 = M_{am}$, $R = 8.314\ \mathrm{J.K}^{-1}.\mathrm{mol}^{-1}$ is the specific gas constant, $\overline{\tau}_{ij} = 2\mu\overline{e}_{ij}$ is the viscous stress tensor for Newtonian fluids with $\overline{e}_{ij} = \frac{1}{2}(\frac{\partial \tilde{u}_i}{\partial x_j} + \frac{\partial \tilde{u}_j}{\partial x_i}) - \frac{1}{3}\delta_{ij}\frac{\partial \tilde{u}_k}{\partial x_k}$ and μ is the mixture dynamic viscosity calculated as a function of the mass fraction and fluids physical properties as in [11, 15],

δ_{ij} the Kronecker symbol and $g_j = (0, 0, -g)$ the gravity vector. The evolution of the mixture's viscosity and density versus the helium mass fraction are presented in figure 2.

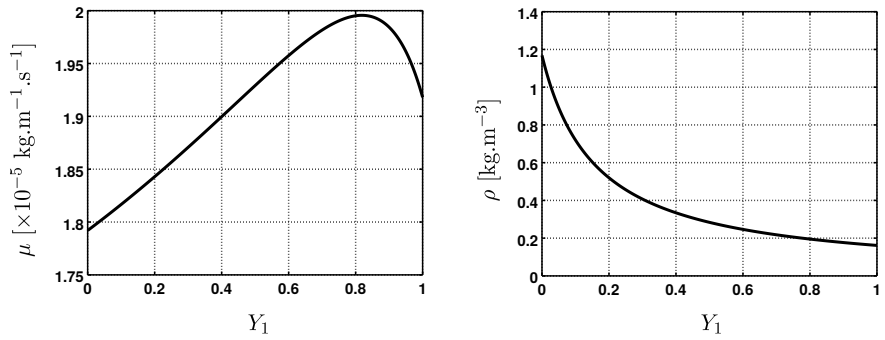

FIG. 2: Evolution of the mixture physical properties as a function of the helium mass fraction Y_1. Left: dynamic viscosity μ, right: density ρ.

We use the classical Smagorinsky model to close the additional sub-grid scale (SGS) terms appearing in equations (1) and (3). Thus, the Reynolds stress $\overline{\tau}_{ij}^{\mathrm{SGS}}$ is expressed as

$$\overline{\tau}_{ij}^{\mathrm{SGS}} = \overline{\rho}(\tilde{u}_i\tilde{u}_j - \widetilde{u_i u_j}) = 2\mu_{\mathrm{SGS}}\overline{e}_{ij}. \tag{5}$$

The SGS dynamic viscosity μ_{SGS} is calculated as

$$\mu_{\mathrm{SGS}} = \overline{\rho}(C_s\Delta)^2\sqrt{2\ \overline{e}_{ij}\overline{e}_{ij}}, \tag{6}$$

where Δ is the filter width taken to be $(\delta_x\delta_y\delta_z)^{1/3}$and δ_x, δ_y and δ_z are the effective mesh spacing [9, 16].
The unresolved turbulent scalar flux $\overline{\xi}_i^{\mathrm{SGS}}$ is modelled by the gradient-diffusion hypothesis as

$$\overline{\xi}_i^{\mathrm{SGS}} = \overline{\rho}(\tilde{u}_i\tilde{Y}_1 - \widetilde{u_i Y_1}) = \frac{\mu_{\mathrm{SGS}}}{Sc_{\mathrm{SGS}}}\frac{\partial\tilde{Y}_1}{\partial x_i}. \tag{7}$$

The Smagorinsky coefficient C_s and the turbulent Schmidt number Sc_{SGS} are considered constant and uniform throughout the whole domain; 0.18 and 0.7 respectively [17, 18]. In the sequel, although denoting filtered quantities, the averaging symbols " $\bar{}$ " and " $\tilde{}$ " are removed for simplicity.

C. Post-treatment quantities

We denote by $< \cdot >_t$, $\mathrm{rms}\{\cdot\}_t$ respectively the time averaged and the root mean square (rms) quantities, calculated for a considered quantity $\varphi(t)$ as

$$< \varphi(t) >_t = \frac{1}{t - t_{\mathrm{start}}}\int_{t_{\mathrm{start}}}^{t}\varphi(t)dt \quad \text{and} \quad \mathrm{rms}\{\varphi(t)\}_t = \left(\frac{1}{t - t_{\mathrm{start}}}\int_{t_{\mathrm{start}}}^{t}(\varphi'(t))^2 dt\right)^{1/2}, \tag{8}$$

where t_{start} corresponds to the starting time of the statistical recordings and φ' is the fluctuating part of φ defined as $\varphi'(t) = \varphi(t) - < \varphi(t) >_t$.

The autocorrelation is thus calculated for a time lag τ as

$$r(\tau) = \frac{< \varphi'(t).\varphi'(t+\tau) >_t}{< \varphi'(t)^2 >_t}. \tag{9}$$

For N independent uncorrelated samples of φ, we define the statistical error as

$$\mathrm{Err}(\varphi) = \frac{\mathrm{rms}\{\varphi(t)\}_t}{\sqrt{N}}. \tag{10}$$

To determine the average fluctuations for a quantity φ at a fixed position in space, a normalized

$$\varphi'' = \frac{\mathrm{rms}\{\varphi(t)\}_t}{< \varphi(t) >_t} \tag{11}$$

is used. The volumetric and helium mass flow-rates crossing each vent are calculated respectively as

$$Q_v^i = \int_{\partial\Omega_{out}^i} u_1 d\sigma \quad \text{and} \quad q_{He}^i = \int_{\partial\Omega_{out}^i} \rho_{in} X_1 u_1 d\sigma, \tag{12}$$

where $i = \{bot, top\}$ and $\partial\Omega_{out}^{bot}$, $\partial\Omega_{out}^{top}$ denote the surface area of the bottom and top vent respectively. X_1 is helium volume fraction defined as $X_1 = (\rho - \rho_{am})/(\rho_{in} - \rho_{am})$.

The total mass of helium inside the cavity with volume V is

$$\mathcal{M}_{He} = \int_V \rho_{in} X_1 dV. \tag{13}$$

We denote the kinetic energy by E_k where $2E_k = \sum_i u_i^2$.

D. Numerical methods

The system of equations is solved in a sequential way at each time iteration using a semi-implicit scheme, which treats implicitly the diffusion terms and explicitly the convective ones. Thus, the time step δt at each iteration is selected to satisfy the convective Courant-Friedrichs-Lewy condition $\mathrm{CFL}_{\mathrm{conv}}$ (maximum reached in our simulations takes $\delta t_{\max} \approx 4.5 \times 10^{-4}$ s). The discretization employs a Finite Difference Volume (FDV) method on a staggered grid [19]. The temporal discretization is performed using a second order Range-Kutta (RK2) scheme. The spatial discretization for all derivative terms is carried out by a second ordered centered scheme except for the convective term of the species equation (1) where a third order quadratic upstream interpolation for convective kinematics (QUICK) scheme is used to ensure the monotonicity property and that $Y_1 \in [0, 1]$. The linear systems resulting from implicit treatment of the diffusion terms are solved by the iterative conjugate gradient method (CGM).

To solve the pressure-velocity problem, an incremental projection method is employed where the variable of the Poisson equation is the pressure increment $\phi = P^{t+\delta t} - P^t$ which is solved by an iterative symmetric successive over relaxation (SSOR) method. The pressure increment ϕ is finally

used for correcting the velocity field over the domain to satisfy the divergence constraint obtained from equation (4) and expressed as

$$\frac{\partial u_i}{\partial x_i} = -\frac{1}{\rho}\frac{D\rho}{Dt}, \tag{14}$$

where $\frac{D}{Dt} = \frac{\partial}{\partial t} + u_i \cdot \frac{\partial}{\partial x_i}$ is the total differentiation operator.

At the initial state, the whole cavity is filled with pure air at rest ($Y_1 = 0$ and $\mathbf{u} = 0$). The boundary conditions are the following: at the inlet boundary $\partial\Omega_{in}$ situated at the bottom end of the pipe, a fixed convective mass flux equal to $\rho_{in}Q$ ($Q = 5$ Nl/min) is imposed with flat profiles for $\rho = \rho_{in}$ and $Y_1 = 1$, whereas a parabolic profile is imposed for $\mathbf{u}$. On the wall boundaries $\partial\Omega_w$, a no-slip boundary condition is applied for $\mathbf{u}$ with a homogeneous Neumann condition for all the scalars ρ, Y_1 and P. At the outlet boundaries $\partial\Omega_{out}$, a fixed pressure $P = \rho_{am}gz$ is imposed for a considered height z with a homogeneous Neumann condition for $\mathbf{u}$. A homogeneous Neumann condition is imposed on ρ and Y_1 if $\mathbf{u}.\hat{\eta} \geq 0$; $\hat{\eta}$ is the outward unit normal at the outlet surfaces. Otherwise, the Dirichlet conditions $\rho = \rho_{am}$ and $Y_1 = 0$ are imposed.

E. Numerical set-up and validation

We perform numerical computations on four different configurations labelled from 1 to 4 using the CEA TRUST-TrioCFD code in the MPI parallel version [19]. In configuration 1, the outlet boundary condition is directly imposed at each vent surface. However, this is not the case for the three other configurations where an exterior domain, of different dimensions, is directly attached to outer vent surfaces and therefore moving the outlet boundary away from the cavity. The exterior domain has a horizontal extension Lx, span-wise length $L + (2 \times Ly)$ and a height $H + (2 \times Lz)$. A summary of the considered configurations can be read from table II.

Configuration	**Exterior**	Lx **[cm]**	Ly **[cm]**	Lz **[cm]**	**Cell numbers**	**MPI procs**
1	No	-	-	-	1,117,204	24
2	Yes	2.6	1.5	1.3	2,163,268	40
3	Yes	4	1.5	2	2,858,668	54
4	Yes	6	1.5	3	4,038,796	80

TABLE II: Descriptions of the computational domains.

A uniform unstructured cubic mesh (per block) has been used with a cell step size of $\delta = 7 \times 10^{-4}$ m in each direction. Following the work of Chhabra et al. in [20], the Kolmogorov length scale can be estimated as $\eta = 2.1 \times 10^{-4}$ m ($\delta/\eta = 3.3$). We keep δ constant in all the four configurations. The origin of the Cartesian system $\mathcal{O}(0, 0, 0)$ is placed at the center of the top injection pipe as seen in figure 1. A layer of 5×10^{-3} m width around the vents in configurations 2 to 4 is imposed with wall boundary condition to take into account the thickness of the plexi-glass in the real experiment. In figure 3, we present a sketch of the considered computational domains. Red surfaces indicate the position of $\partial\Omega_w$, $\partial\Omega_{in}$ in yellow and finally the blue surfaces for $\partial\Omega_{out}$. The grid inside the pipe is identical in the four configurations (subfigure (a)). Subfigure (b) represents the computational domain of configuration 1. Subfigure (c) indicates the $\partial\Omega_w$ of configurations 2 to 4 where a sketch of the complete domain is sketched in subfigure (d).

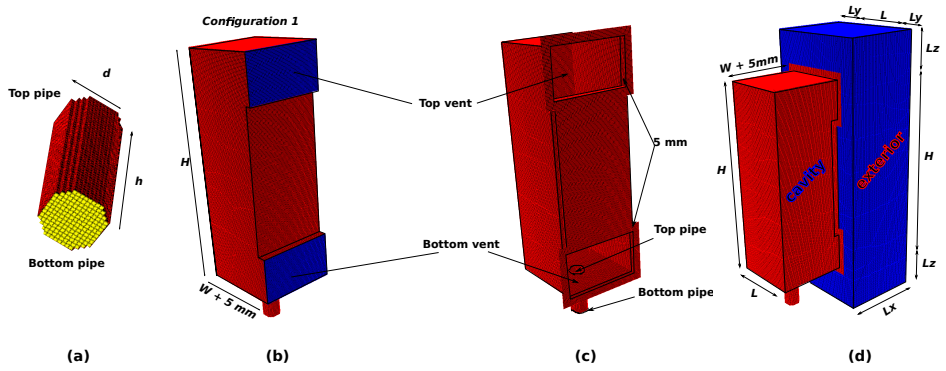

FIG. 3: 3D sketch of the computational domains: $\partial\Omega_w$ on red surfaces, $\partial\Omega_{in}$ on yellow surface and $\partial\Omega_{out}$ on blue surfaces.

A grid convergence study has been carried out for configuration 1 on seven different uniform meshes of step size decreasing with a geometric factor $r = 1.3$ from 2×10^{-3} m to 4.14×10^{-4} m. The mean values of the helium mass fraction Y_1 and velocity magnitude $|\mathbf{u}|$ show satisfactory converged LES results starting from a grid of step size of 7 $\times10^{-4}$ m. However, we note that the convergence of the rms is much slower, but satisfactory converged values has been reached.

For all configurations, we have simulated a physical time of 110 seconds. A quasi-steady state solution is identified by tracking the time evolution of the flow variables at fixed points in the computational domains. We have seen that the time required to attain a quasi-steady state solution is dependent on the configuration and thus can be illustrated by looking to the evolution of the velocity magnitude at a probe situated in the middle of the top vent (figure 4).

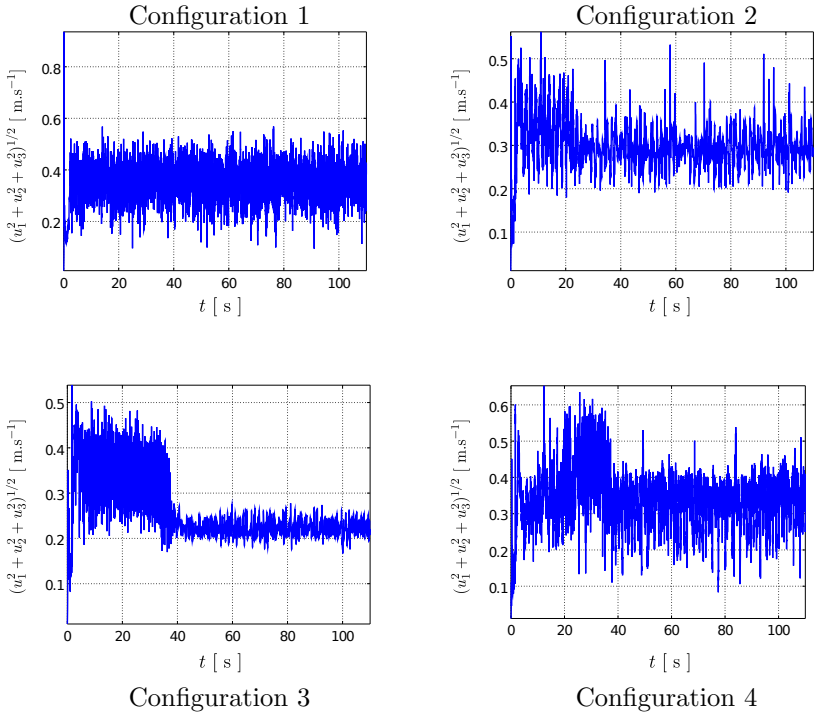

FIG. 4: Velocity magnitude evolution versus time at a fixed position in the middle of the top vent ($x = 2.45$, $y = 0$ and $z = 13.5$ cm). Configurations 1 to 4.

The statistical fields have been recorded starting from $t_{\text{start}} = 80$ s with a frequency $f = 1/\delta t$ Hz, where we assume that the transient solution is already covered.

III. RESULTS

A. Influence of the outlet boundary conditions

To study the influence of the outlet boundary condition on the flow inside the cavity, numerical computations have been performed on the four configurations already presented in subsection II E. A detailed study on this issue can be reviewed from the work of Saikali et al. in [21].

The flow pattern inside the cavity has been noted to have some similar behavior independent of the considered computational domain. First, the distribution of the time averaged kinetic energy is almost the same. In all configurations, $< E_k >_t$ is mainly concentrated inside the bottom jet axis and that it is more diffusive in a large part of the upper cavity facing the vents, where the buoyancy forces are dominant. Second, in addition to the helium jet injected from the pipe, we observe that in all configurations, pure air enters the cavity from outside through the bottom vent. It impacts the axis of the jet and entrains with helium while rising to dilute an air-helium mixture in the upper part of the cavity. A part of this mixture leaves the cavity through the top vent while the remaining goes into a recirculating motion. The air-helium impact in the bottom part of the cavity is reflected on the jet axis by a deviation from the central position of the cavity towards the left wall, breaking by that the circular jet structure. This deformation can be illustrated by $< X_1 >_t$ in a horizontal plane (figure 5).

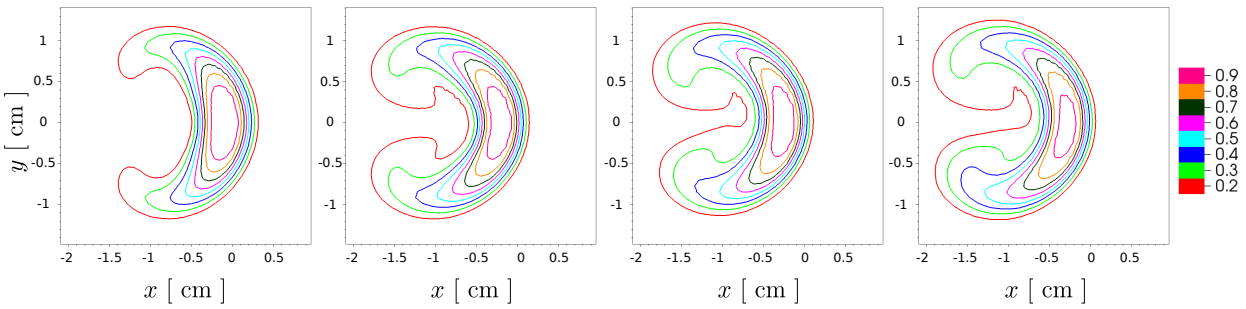

Configuration 1 Configuration 2 Configuration 3 Configuration 4

FIG. 5: Time averaged flow pattern in the horizontal xy-plane ($z = 2$ cm) for configurations 1 to 4: line contours of the time averaged volume fraction $< X_1 >_t$.

It has been noted that there is a significant influence on the flow inside the cavity while considering the different configurations. First, we see that the bending of the jet axis towards the wall facing the vents is strengthened when taking an exterior domain into consideration. This inclination plays an important role on the distribution of helium inside the cavity where it has been found that configurations 2 to 4 contain higher levels of helium in the upper part of the cavity compared to configuration 1. However, due to the difference of the structure of the jet axis, the global mass of helium $\mathcal{M}_{He}$ inside the cavity is found to be higher in configuration 1 (figure 6).

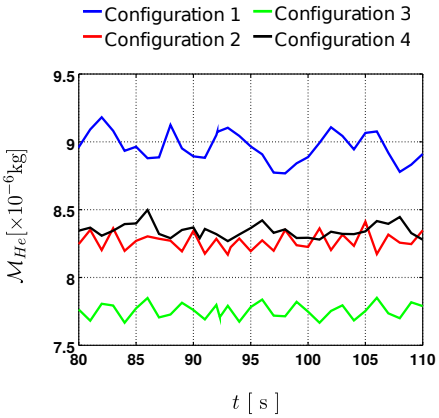

FIG. 6: Time evolution of the helium total mass $\mathcal{M}_{He}$ inside the cavity for configurations 1 to 4.

As a consequence, it has been observed that the volumetric flow-rates passing through the bottom and top vents respectively Q_v^{bot}, Q_v^{top} take the highest absolute values in configurations that account an exterior domain. This result is not surprising as far as we consider a constant volumetric flow-rate at the injection.

It has been found that the size of the exterior domain can affect the behavior of the flow near the top vent region. In particular, it seems that the reduced size in configuration 2 blocks the flow at the top exit where horizontal helium stratification is observed in the upper exterior region. This issue was improved by increasing the size of the exterior domain where the mixture can leave freely the domain with the help of the buoyancy. This can be seen on figure 7 which shows the time averaged distribution of the helium volume fraction $< X_1 >_t$ in the vertical mid plane for all cases.

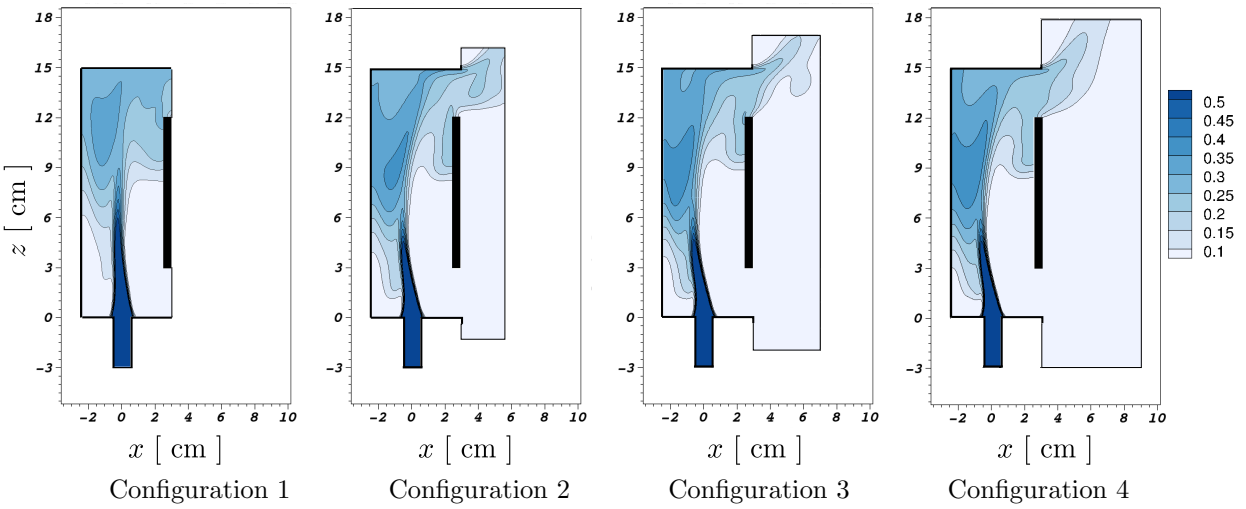

FIG. 7: Time averaged flow pattern in the vertical mid xz-plane ($y = 0$) for configurations 1 to 4: iso-contours of the time average volume fraction $< X_1 >_t$.

In addition, by revisiting figure 4, we can note that the size of the exterior domain can influence the magnitude of the fluctuating field. To illustrate, we present the rms of the velocity magnitude $\mathrm{rms}\{|\mathbf{u}|\}_t$ in the vertical mid xz-plane (figure 8). The values in all cases are dominant in the upper part of the cavity, however particularly the greatest are devoted to configurations 1 and 4.

The oscillations are of smaller magnitudes in the remaining configurations with least recorded in configuration 3.

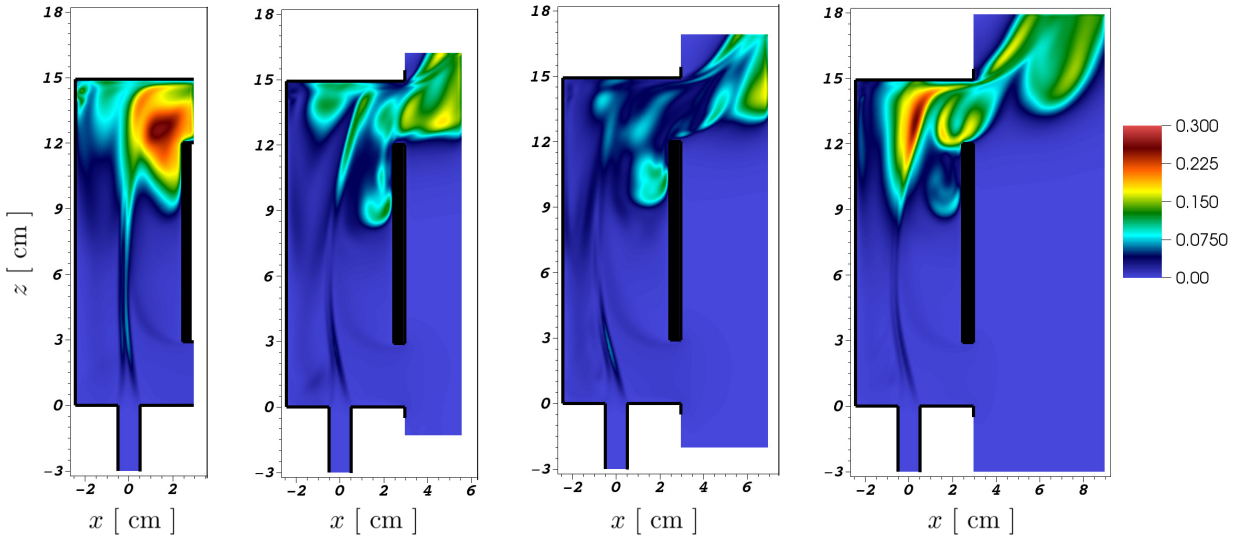

FIG. 8: rms$\{|\mathbf{u}|\}_t$ iso-contour plot in the vertical mid xz-plane ($y = 0$) for configurations 1 to 4.

From this variation, we conclude that a convergence study on the size of the exterior domain is required for a good statistical analysis and is to be carried out in a future work.

B. Validation against PIV

To validate the numerical results and to conclude on the configuration that can be considered as the best in representing the real experiment, we use the available PIV measurements at the bottom region of the cavity in the vertical mid xz-plane. The vertical profiles of the time averaged $< u_1 >_t$ located at the bottom vent in the considered plane are plotted in figure 9.

Configuration 1 shows almost a virtual uniform profile which differs to what is obtained by configurations 2 to 4, where almost similar profiles are noted whatever the configuration with an exterior domain is considered. The influence of the size of the exterior domain is mainly sensitive at the extremities where the highest absolute values have been recorded. We see that the profile obtained from the experiment takes almost the same profile as those obtained with configurations 2 to 4 where the values remain within the experimental measurement error (0.02 m.s^{-1} absolute error). However, the best results are found using configuration 4. This is confirmed by looking at the lower region near the injection where we see the similar flow patterns obtained from the simulation of configuration 4 and from the real experiment (figure 10). The time averaged contour lines of the velocity magnitude in the mid xz-plane $(< u_1 >_t^2 + < u_3 >_t^2)^{1/2}$ show great similarities.

In what follows, the analysis is carried out on the quasi-steady state solution of configuration 4.

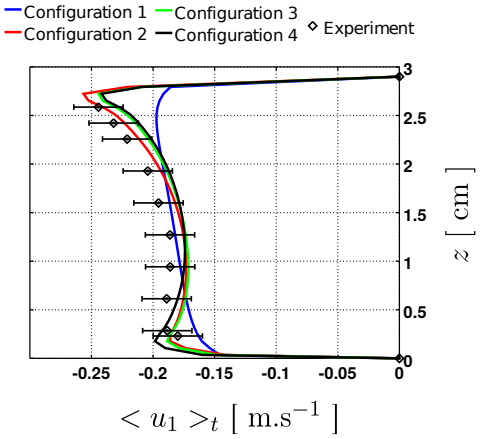

FIG. 9: Time averaged flow pattern in the vertical yz-plane ($x = 2.95$ cm) at the bottom vent for configurations 1 to 4 and experimental PIV data: $< u_1 >_t$ mid-vertical profile ($y = 0$)

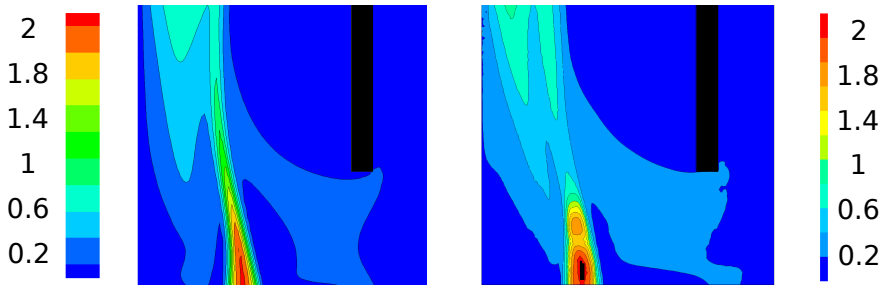

Configuration 4 Experiment

FIG. 10: Time averaged flow pattern in the lower part of the vertical mid-plane ($y = 0$): xz-plane time averaged velocity magnitude iso-contours $(< u_1 >_t^2 + < u_3 >_t^2)^{1/2}$. Left: configuration 4, right: PIV measurement.

C. 3D flow description

We present the 3D flow inside the cavity by considering the simulation of configuration 4. The flow pattern is illustrated by the evolution of the instantaneous helium volume fraction X_1 as a function of time (figure 11).

The cavity is initially filled with air at $t = 0$ s. After the first time iteration, the helium mass is convected inside the cavity and the buoyant jet rises, pushing the air in all directions by a rotational motion. The jet/top wall impact is firstly observed at $t = 0.21$ s (sub-figure (a) of 11). Afterwards, and due to the continuous injection, the flow spreads all over the ceiling, impacts the lateral walls from three sides and descend in a rotational form. This behavior allow the dilution of helium in air. The forth direction corresponds to the top vent where a part of the mixture leaves the cavity.

In the first 0.5 seconds of the simulation, the flow is described as a laminar starting buoyant jet which is stable, symmetric and aligned with the vertical direction. As time advances and to ensure the conservation balance principle, fresh air enters the bottom vent and impacts the jet axis with a significant velocity causing the jet to deviate towards the wall facing the vents. This is firstly

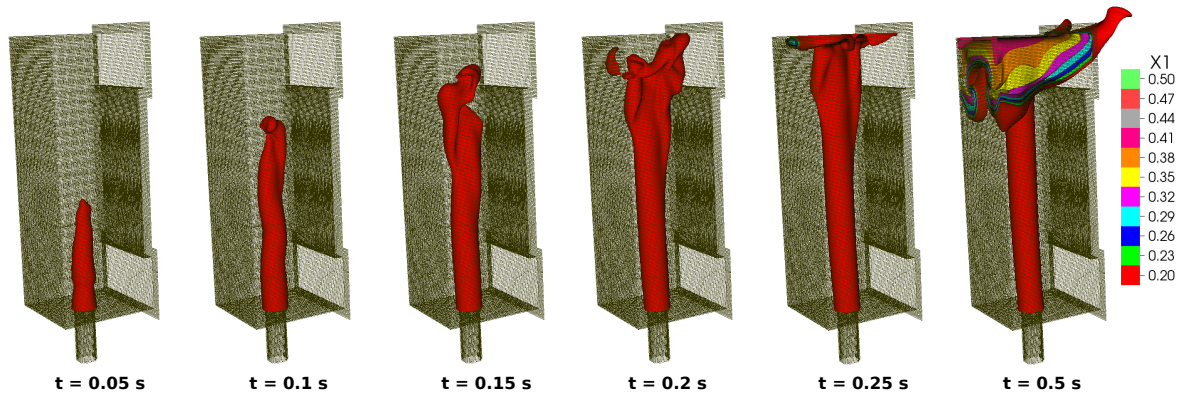

(a)Laminar starting buoyant jet: symmetrical, centralized jet axis

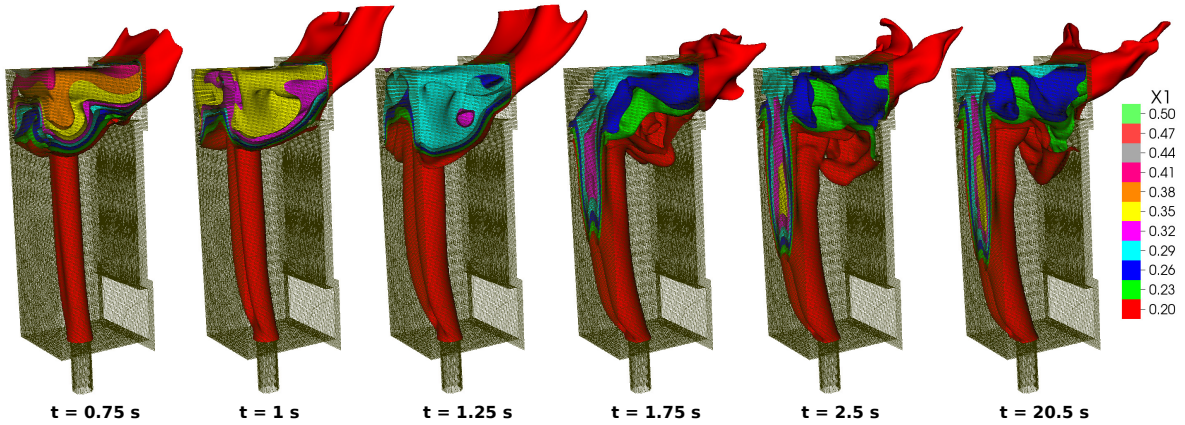

(b)Laminar-turbulent transitional buoyant jet: bended, deformed jet axis

FIG. 11: 3D flow pattern: time evolution of instantaneous X_1 iso-surface contours.

observed at $t = 0.75$ s and is strengthened with time (sub-figure (b) of 11). After the impact, the flow spreads symmetrically with respect to the axis in two parts. In each part, two opposite vortices are created: one continues to recirculate near the corner of the cavity and the other one circumvents the jet axis until it collides with the one symmetrically coming from the other side of the jet. When these two counter-rotating vortices collide, they form a dipole that accelerates and enters within the jet axis causing a deformation of the initial circular structure. Finally, the dipole is convected upward and an other dipole forms repeating the same mechanism. This behavior can be illustrated by the time averaged velocity stream lines in the xy-horizontal plane crossing the bottom vent (figure 12).

Rayleigh-Taylor instabilities grow with the jet due to the impact of air with the light helium. These instabilities create high fluctuations that induce a laminar-to-turbulent transition. This is confirmed by the instantaneous X_1 fields mainly in the upper part of the cavity, where the distribution changes significantly in each time snap-shot. Outside the jet, we locate fluctuations reaching approximately 60% for the velocity magnitude field. A difficulty at this step is to identify whether the height of the cavity is enough so that the flow develops into a complete turbulent regime and the issue is kept for our future investigations.

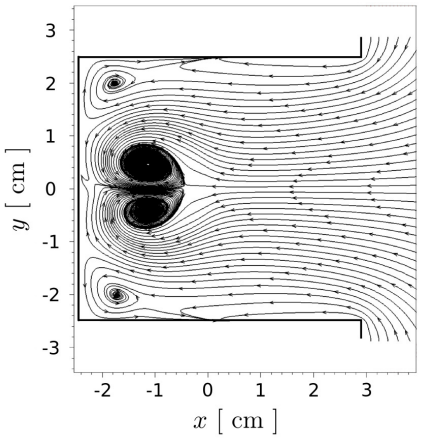

FIG. 12: Time averaged flow pattern in the horizontal xy-plane ($z = 2$ cm): stream lines of $< \mathbf{u} >_t$.

D. Helium stratification

To understand the air-helium mixing-dispersion phenomenon inside the cavity, we look at the time averaged helium volume fraction distribution. Eight equidistant points are considered, fixed in the xy-horizontal plane. The corresponding position and the label (A to H) can be seen in figure 13 (left). The thick red point denotes the projection onto the origin $\mathcal{O}$.

The vertical profiles of $< X_1 >_t$ located at the eight points are plotted in figure 13 (middle). Solid black line corresponds to the distribution along the jet axis. We observe two distinct behaviors of the profiles which take small compared to higher concentrations of helium. Above an approximate height of $z \approx 6.2$ cm, highest helium concentrations are situated inside the jet and along the vertical position through point E. The remaining profiles along points A to D and F to H are almost similar and thus their average is calculated and represented by the thick red line (figure 13 (right)).

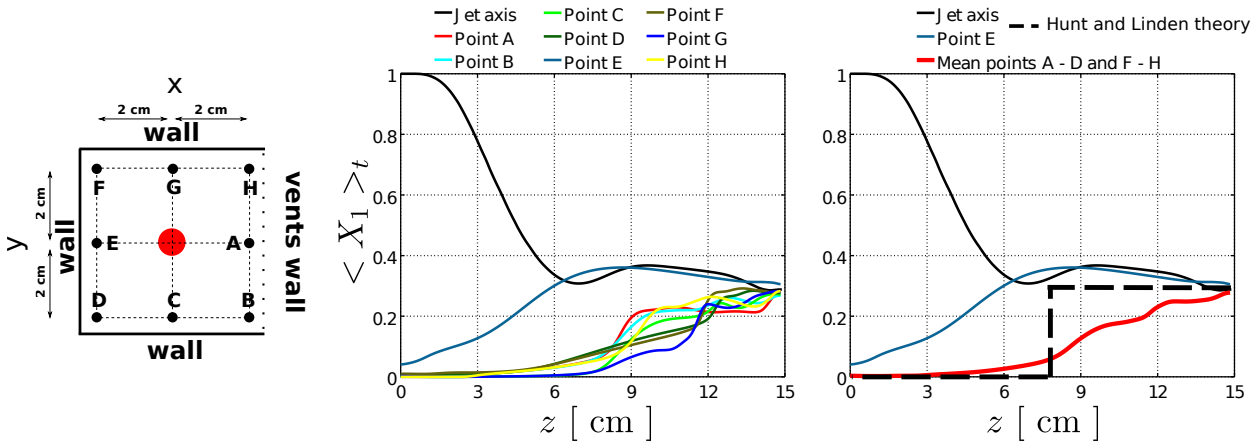

FIG. 13: Left: cavity top view, middle and right: $< X_1 >_t$ vertical profiles. Thick red line denotes the average vertical profile for points A to D and F to H. Thick black dashed line corresponds to the estimated neutral plan according to the theory of Hunt and Linden.

Both, the mean profile (thick red line) and that along point E show almost a virtual uniform profile (plateau). This means that a homogeneous mixture layer is situated in the upper part of the cavity. However, the thickness of the layer is not uniform as it starts approximately from $z \approx 6.2$ cm in the region of the point E (composed of 33 % pure helium in average) compared to $z \approx 12.4$ cm (composed of 28 % pure helium approximately) in the remaining portion.

The thick black dashed line corresponds to an estimation on the position of the homogeneous layer, carried by Bernard-Michel et al. in [22], using the theory of Hunt and Linden [23]. We see that the configuration in our case is not situated in the framework of the considered theory which predicts a layer of uniform thickness in the upper part, although the maximum concentration of helium at the top (29%) matches well.

E. Statistical post-treatment

In this section, we present a primary statistical post-treatment using the quantities defined in section II C. To identify the approximate height at which the transition from laminar to turbulence starts, we plot the vertical profile of the normalized averaged helium local fluctuations X_1'' along the jet axis (figure 14). According to the work of Plourde et al. in [24], we assume that the transition to turbulence is located where the first maximum along the vertical profile is reached. For our configuration, this transition starts approximately at $z = 4.4$ cm, as we could see in figure 14 (left). The height is in accordance with the PIV measurements of the velocity magnitude (see figure 14 (right).

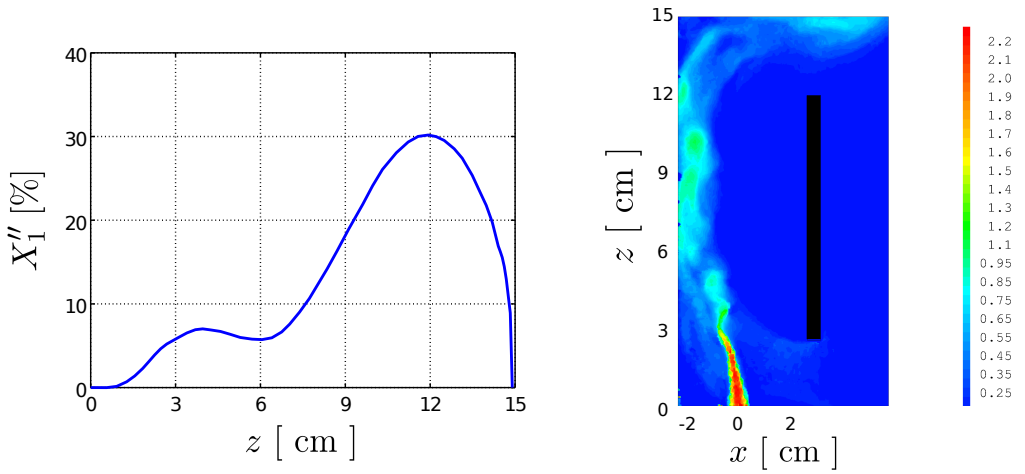

FIG. 14: Transitional regime identification. Left: Normalized averaged helium volume fraction fluctuations X_1'' along the jet axis, right: PIV instantaneous velocity magnitude field.

To specify the accuracy of the statistical data and identify the bounds of the numerical errors, we calculate the auto-correlation function (ACF) for the velocity magnitude and the helium mass fraction. The ACF has been evaluated at a point in the top vent ($x = 2.45$, $y = 0$ and $z = 14$ cm), where the highest fluctuations are recorded. The fields have been recorded as a function of time with a frequency of 100 Hz. Figure 15 is devoted to the ACF of Y_1.

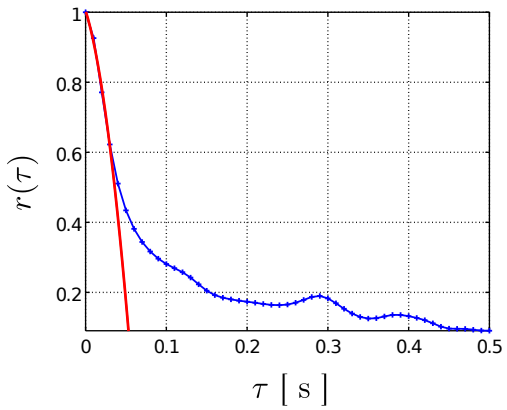

FIG. 15: ACF(Y_1) at a point situated in the mid xz-plane at the top vent ($x = 2.45$, $y = 0$ and $z = 14$ cm). Red line correspond to a parabola fit near the origin.

The correlation rapidly decreases with the time delay τ. A good quadratic polynomial is fitted around the origin and thus plotted on the same graph (red line). According to the definition of the Taylor micro-scale λ_f in the book of Pope [25], we observe $\lambda_f \approx 0.05$ s (intersection of the fitted parabola with the time delay axis). According to the recorded frequency, each consecutive 5 samples are considered to be in correlation.

The convergence of $r(\tau)$ towards zero is rather long since it has been reached for a time delay of about 40 s, the total time of the statistical recordings in our simulation. This high delay is justified by a low frequency flapping motion that occurs at this position. Further investigations are to be carried out in a future work.

In practice, 40 s of statistics corresponds to 800 uncorrelated samples. Thus, the statistical error on Y_1 at the considered location is estimated to be $\text{rms}\{Y_1(t)\}_t/\sqrt{800} \approx 0.034\%$ on Y_1 (0.65% on the magnitude of $\mathbf{u}$).

F. Fine LES resolution

In section II E, we have pointed that according to a carried grid convergence study, we require a cell size δ for a good accuracy. In this section, we show that the numerical simulation performed on such a grid is a coarse direct numerical simulation (DNS); or in other words a fine LES. To illustrate, we consider the mid vertical xz-plane and we perform a similar LES qualification to that carried out by Maragkos et al. in [26].

The ratio of the SGS to mixture kinematic viscosity is calculated. Globally, we observe from figure 16 that ν_{SGS}/ν takes a maximum of 0.3 in the quasi-steady state solution inside the cavity (the modeled viscosity in the exterior domain is not taken into account). The maximum of the ratio confirms that a fine LES has been carried out.

An instantaneous LES resolution can be illustrated at time $t = 96$ seconds in figure 17. We can clearly note that the highest values of ν_{SGS} are recorded at the jet axis and in the recirculating zones located mainly in the top left corner and in the region between the jet-left wall (figure 17,

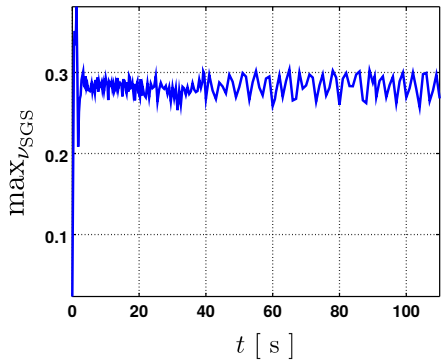

FIG. 16: The maximum evolution of the SGS to mixture viscosity's ratio (ν_{SGS}/ν) in the vertical mid xz-plane ($y = 0$).

left). This is confirmed as far as, by construction, the Smagorinsky's model is linearly dependent of the velocity gradients.

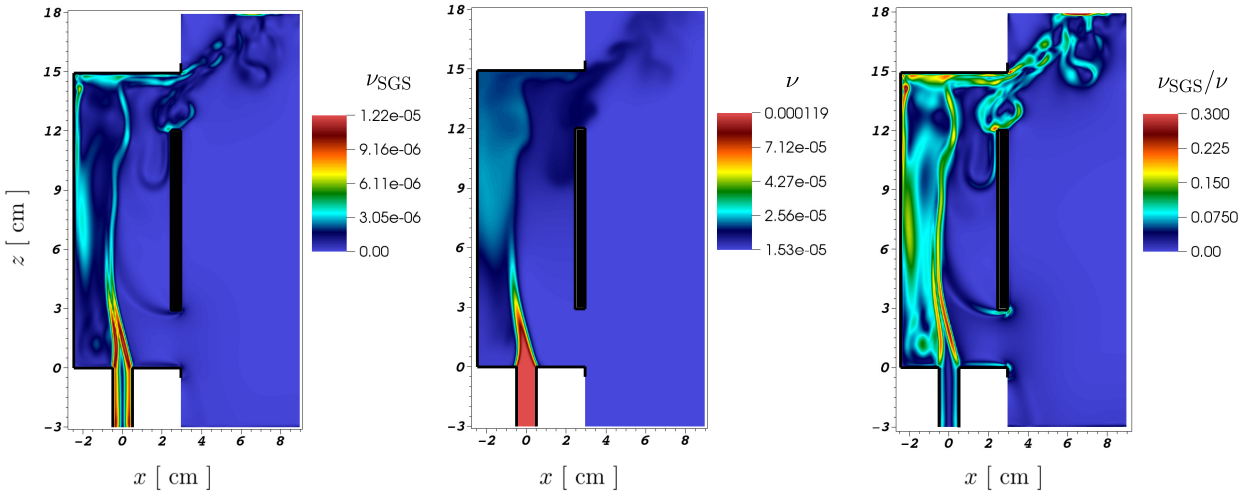

FIG. 17: Instantaneous iso-contour plots at $t = 96$ seconds in the vertical mid xz-plane ($y = 0$). Left: SGS kinematic viscosity ν_{SGS}, middle: mixture kinematic viscosity ν (levels in a log scale), right: ratio ν_{SGS}/ν.

The importance of the modeled viscosity can be viewed from the ratio (figure 17 right). Three horizontal profiles are sketched in figure 18 (left) approximately at the bottom ($z = 1.2$ cm), the middle ($z = 7.8$ cm) and the top of the cavity ($z = 14.2$ cm). The peaks clearly indicate the position of the jet edges and flow recirculating zones. The ratio is almost the same in the remaining unsteady regime.

The Kolmogorov length scale η_{LES} and the ratio of the grid spacing δ to η_{LES} have been estimated and an instantaneous field is considered in the vertical mid xz-plane (figure 19). Along the three previously considered heights, we plot the horizontal profiles of this ratio (figure 18, right).

$\eta_{\mathrm{LES}} = (\nu^3/\epsilon)^{0.25}$ is estimated from the obtained LES results, where the total dissipation rate is evaluated as $\epsilon = 2(\nu_{\mathrm{SGS}} + \nu)(e_{ij} : e_{ij})$, " : " being the tensor contraction operator.

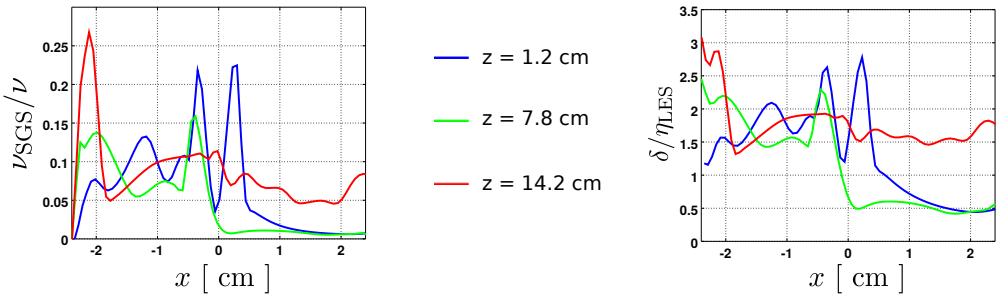

FIG. 18: Horizontal profiles in the vertical mid xz-plane ($y = 0$). Left: ratio of ν_{SGS}/ν, right: ratio of the grid spacing δ to Kolmogorov length scale η_{LES}.

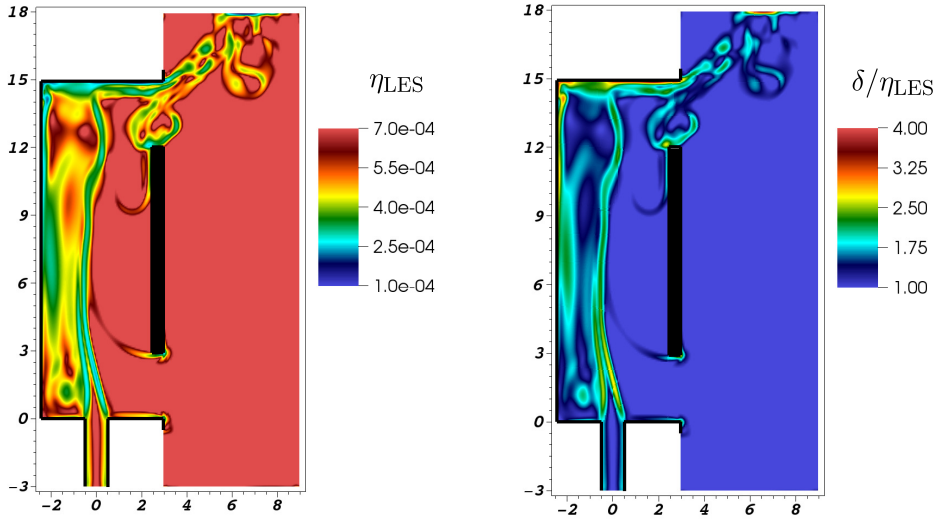

FIG. 19: Instantaneous iso-contour plots at $t = 96$ seconds in the vertical mid xz-plane ($y = 0$). Left: estimated Kolmogorov length scale η_{LES}, right: ratio of the grid spacing δ to Kolmogorov length scale η_{LES}.

We note that η_{LES} is dependent on the position and thus on the flow pattern, although the maximum ratio δ/η_{LES} is figured out to be 3.5, which is relatively small in the art of LES [26]. Assuming that the Smagorinsky model is correctly representing the unresolved scales and that the estimation of ϵ is good, we can say that the LES is correctly representing the flow.

From the figures, the smallest Kolmogorov length scales are located at the jet edges (peaks on the horizontal profiles) and in the recirculation regions near the left wall facing the vents. On contrary, in the region near the bottom vent where the flow is almost uniform, we see that the mesh is enough to capture the small scales without requiring an eddy-viscosity model.

IV. DISCUSSIONS AND CONCLUDING REMARKS

The flow of an air-helium buoyant jet in a two vented enclosure was modeled numerically by LES using the classical Smagorinsky SGS model. Numerical simulations were carried out on four

configurations having the same cell size. Analyses on time averaged quantities show a lot of similarities in the flow pattern for all configurations; basically the kinetic energy distribution and the deformation of the jet axis. However, significant discrepancies have been seen on the helium distribution in the cavity and on the global averaged quantities like volumetric and mass flow-rates. It has been shown that configuration without exterior domain underestimates the volumetric flow rate of fresh air entering the cavity and thus overestimates the total mass of helium. Comparisons between experimental and numerical simulations in a region near the bottom vent seems satisfactory when taking into account an exterior domain. The air-helium mixing-dispersion has been analyzed by vertical profiles of the time averaged volume fraction. A homogeneous mixture layer at the top of the cavity is identified with a non uniform thickness, and thus can not be predicted from the theory of Hunt and Linden. The time averaged ratio of the modeled to the mixture viscosity indicates that the performed simulation is a fine LES.

Mainly, a convergence study on the size of the exterior domain remain in our future perspectives. In a next step, we look for defining the correct boundary conditions that can be imposed directly on the vents without modelling an exterior region, and thus represent correctly the flow. The convergence of the ACF requires further investigation. Analysis on the transitional-turbulent regime is to be carried out in a future work.

Further experimental PIV measurements are in progress allowing a more detailed comparison in the whole domain.

V. ACKNOWLEDGMENTS

The simulations reported in this paper have been performed on the CEA local cluster CALLISTO. The authors would like to gratefully thank the TRUST support team and Gautier Fauchet for the interesting discussions and support.

---

[1] H. L. Tran, A. Sergent, G. Bernard-Michel, and P. Le Quere, in *Progress in safety of hydrogen technologies and infrastructure: enabling the transition to zero carbon energy. Proceedings of the 5th International Conference on Hydrogen Safety (ICHS). 9-11 Sept 2013, Brussels, Belgium* (2013), URL `http://www.ichs2013.com/images/papers/236.pdf`.

[2] B. Cariteau and I. Tkatschenko, *Experimental study of the concentration build-up regimes in an enclosure without ventilation*, international journal of hydrogen energy **37**, 17400 (2012).

[3] C. J. Chen and W. Rodi, *Vertical turbulent buoyant jets: a review of experimental data*, NASA STI/Recon Technical Report A **80** (1980).

[4] W. Rodi, *Turbulent buoyant jets and plumes*, vol. 3 (Pergamon press Oxford, 1982).

[5] W. Baines and J. Turner, *Turbulent buoyant convection from a source in a confined region*, Journal of Fluid mechanics **37**, 51 (1969).

[6] W. Mell, A. Johnson, K. B. McGrattan, and H. R. Baum, *Large eddy simulations of buoyant plumes*, Chemical and Physical Processes in Combustion pp. 187–190 (1995).

[7] R. Satti, K. Pasumarthi, and A. Agrawal, in *42nd AIAA Aerospace Sciences Meeting and Exhibit* (2004), p. 1317.

[8] R. Friedrich and W. Rodi, *Advances in LES of Complex Flows: Proceedings of the Euromech Colloquium 412, held in Munich, Germany 4- 6 October 2000*, vol. 65 (Springer Science & Business Media, 2002).

[9] G. Blanquart and H. Pitsch, *Large-eddy simulation of a turbulent buoyant helium plume*, Bulletin of the American Physical Society **53** (2008).
[10] R. Kalter, M. J. Tummers, J. B. W. Bettink, B. W. Righolt, S. Kenjereš, and C. R. Kleijn, *Aspect ratio effects on fluid flow fluctuations in rectangular cavities*, Metallurgical and Materials Transactions B **45**, 2186 (2014).
[11] H. L. Tran, Theses, *Numerical modelling of natural convection of binary mixtures: case of a helium buoyant jet in an air-filled enclosure*, Université Pierre et Marie Curie - Paris VI (2013), URL `https://tel.archives-ouvertes.fr/tel-00920867`.
[12] H. N. Najm, P. S. Wyckoff, and O. M. Knio, *A semi-implicit numerical scheme for reacting flow: I. stiff chemistry*, Journal of Computational Physics **143**, 381 (1998).
[13] S. Hamimid, M. Guellal, and M. Bouafia, *Numerical study of natural convection in a square cavity under non-boussinesq conditions*, Thermal Science pp. 84–84 (2014).
[14] B. Müller and B. Muller, *Low mach number asymptotics of the navier-stokes equations and numerical implications* (1999).
[15] C. Wilke, *A viscosity equation for gas mixtures*, The journal of chemical physics **18**, 517 (1950).
[16] M. Pham, F. Plourde, and K. Doan, *Direct and large-eddy simulations of a pure thermal plume*, Physics of Fluids **19**, 125103 (2007).
[17] Z. Cheng, V. Agranat, and A. Tchouvelev, in *Proceeding of the 1st International Conference on Hydrogen Safety* (2005).
[18] N. Panchapakesan and J. Lumley, *Turbulence measurements in axisymmetric jets of air and helium. part 2. helium jet*, Journal of Fluid Mechanics **246**, 225 (1993).
[19] CEA, *TRUST-TrioCFD code version 1.7.4*, `http://www-trio-u.cea.fr`.
[20] S. Chhabra, P. Huq, and A. K. Prasad, *Characteristics of small vortices in a turbulent axisymmetric jet*, Journal of fluids engineering **128**, 439 (2006).
[21] E. Saikali, A. Sergent, G. Bernard-Michel, and C. Tenaud, in *Proceeding of the 23ème Congrès Français de Mécanique* (2017).
[22] G. Bernard-Michel, E. Saikali, and D. Houssin, in *Proceeding of the International Conference on Hydrogen Safety* (2017).
[23] G. Hunt and P. Linden, *The fluid mechanics of natural ventilation-displacement ventilation by buoyancy-driven flows assisted by wind*, Building and Environment **34**, 707 (1999).
[24] F. Plourde, M. V. Pham, S. D. Kim, and S. Balachandar, *Direct numerical simulations of a rapidly expanding thermal plume: structure and entrainment interaction*, Journal of Fluid Mechanics **604**, 99 (2008).
[25] S. Pope, *Turbulent Flows* (Cambridge University Press, 2000), ISBN 9780521598866, URL `https://books.google.fr/books?id=HZsTw9SMx-0C`.
[26] G. Maragkos, P. Rauwoens, Y. Wang, and B. Merci, *Large eddy simulations of the flow in the near-field region of a turbulent buoyant helium plume*, Flow, Turbulence and Combustion **90**, 511 (2013), ISSN 1573-1987, URL `http://dx.doi.org/10.1007/s10494-012-9437-5`.